Fast Finite-Difference Calculation of Eddy Currents in Thin Metal Sheets

James R. Nagel

Department of Metallurgical Engineering
University of Utah, Salt Lake City, UT 84112, USA
james.nagel@utah.edu

Abstract ─ Magnetic excitation of eddy currents in a thin metal sheet is a difficult problem that has many useful applications to scrap metal recycling. Using finite-difference approximations on both the curl and divergence of the current density, we develop a numerical algorithm that is simple to implement, quick to solve, and capable of modeling excitation from arbitrary magnetic field distributions. For the special case of a weakly-induced eddy field, the self-inductance terms can be neglected, resulting in a sparse system matrix that is easily inverted. For a strongly-induced eddy field, self-inductance must be included at the cost of a more complex, denser system matrix. The method is validated against the CST EM Studio software suite and produces nearly identical results on a thin-sheet simulation in only a tiny fraction of the time.

Index Terms ─ Current density, eddy currents, finite-difference method, quasistatics.

I. INTRODUCTION

The excitation of electrical eddy currents in metal objects is a well-known phenomenon with many practical applications. For example, eddy current testing is a form of nondestructive probing that detects the presence of cracks in a metal plate by measuring changes in impedance to a current-carrying coil [1, 2]. Levitation melting is a technology that uses eddy currents to repel particles against gravity to avoid contact contamination with a physical container [3, 4]. Eddy current separation is a popular method for separating nonferrous metal particles from other nonmetallic fluff [5]. Electrodynamic sorting is a recent technology that uses high-frequency electromagnets to separate nonferrous metal particles from other dissimilar metals [6, 7, 8].

For all of its industrial applications, the mathematical theory behind eddy current induction is notoriously complex. Although some canonical problems can be solved analytically [9] (e.g., spheres, cylinders, etc.), many basic geometries are still difficult to model accurately. In particular, the thin metal sheet is especially interesting due to its prevalence among scrap metal particles encountered throughout the recycling industry. Some authors have been able to generate approximate solutions for thin metal rectangles under the assumption of uniform excitation by a magnetic field [10] but only by neglecting the self-inductance of the induced currents. For the purposes of electrodynamic sorting, however, the net force acting on a particle relies on both the nonuniformity of the magnetic field as well as the self-inductance of the induced currents [8, 11].

When analytic solutions are unavailable, the next best alternative is to utilize numerical approximations for the induced eddy currents throughout an object. This is usually accomplished through some variation of the finite-element method (FEM), with many competing formulations to choose from [12, 13]. Generally speaking, however, the majority of such methods tend to fall into one of two distinct categories. The first formalism is commonly referred to as the $\mathbf{A}-\phi$ method because it utilizes on the magnetic vector potential $\mathbf{A}$ and electric scalar potential φ [14]. The second formalism is called the $\mathbf{T}-\Omega$ method because it utilizes the electric vector potential $\mathbf{T}$ and magnetic scalar potential Ω [15].

A key problem with both of these formalisms is the imposition of boundary conditions, which cannot necessarily terminate at the edge of a body of interest [16]. Instead, the simulation must often include a large void of empty space surrounding the particle so that meaningful boundary conditions may be applied far away at near-infinity. As a result, significant computational memory must be devoted to the uninteresting samples of empty space beyond the object of interest. This can be especially wasteful for the case of thin metal sheets, which presumably ought to simplify into much more compact expressions in only two dimensions.

What is needed is a fast, accurate method for calculating the induced eddy current density along a thin metal sheet as it is excited by an arbitrary magnetic field profile. More specifically, we would like a method that only requires sampling along the region of space inside the metal object and that does not waste resources on the empty void of space beyond the particle of interest. To fill that need, this paper reexamines the governing equations of eddy current theory and derives a simplified numerical algorithm accordingly. Rather than invoke the

Submitted On: March 20, 2018
Accepted On: May 19, 2018

use of any specialized potential functions, we may instead solve directly for the desired field components by expressing the problem in terms of divergence and curl. The method shares many similarities with the well-known finite-difference method (FDM), and thus follows a similar derivation to that found in [17]. This makes the algorithm relatively simple to implement by avoiding many of the complex meshing problems typically associated with finite element methods.

II. THEORETICAL BACKGROUND

Figure 1 shows the geometry of interest considered for this work. A rectangular metal sheet with spatially-varying conductivity $\sigma(x,y)$ has length L_x, width L_y, and thickness L_z. The sheet is assumed to be very thin such that $L_z \ll L_x$ and $L_z \ll L_y$. This allows us to consider only the normal component to the magnetic field, since the sheet is too thin to experience any significant excitation by parallel components. We therefore express the impressed magnetic field distribution as $B_i(x,y)\,\hat{\mathbf{z}}$, which is assumed to excite the system in a sinusoidal steady state with angular frequency $\omega = 2\pi f$. Our goal is to solve for the eddy current density $\mathbf{J}(x,y)$ induced throughout the plate.

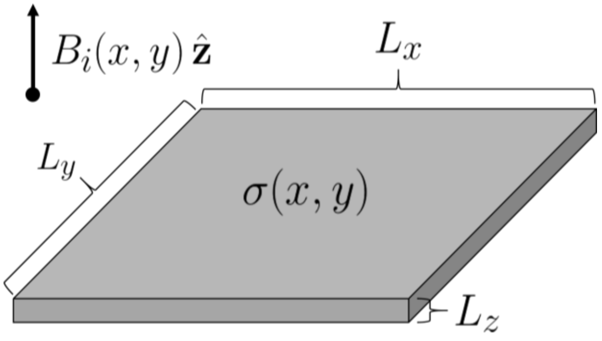

Fig. 1. A thin metal sheet is excited normally by an impressed magnetic field profile $B_i(x,y)\,\hat{\mathbf{z}}$.

We begin with Maxwell's curl equations for linear, isotropic, nonmagnetic media in phasor form. Assuming a phasor convention of $Ae^{j\omega t}$, we let $d/dt = j\omega$. Given a magnetic field intensity $\mathbf{B}$, electric field intensity $\mathbf{E}$, and current density $\mathbf{J}$, Ampere's law states that:

$$\nabla \times \mathbf{B} = \mu_0 \mathbf{J} + j\omega\mu_0\epsilon_0 \mathbf{E}\,, \tag{1}$$

where μ_0 is the permeability of free space and ϵ_0 is the permittivity. In the context of eddy current excitation by time-varying magnetic fields, the last term in Ampere's law is assumed to be negligibly small. This condition is commonly known as the quasistatic approximation and allows us to rewrite:

$$\nabla \times \mathbf{B} \approx \mu_0 \mathbf{J}\,. \tag{2}$$

If we now take the divergence of both sides, the curl term vanishes to produce:

$$\nabla \cdot \mathbf{J} = 0\,. \tag{3}$$

What (3) tells us is that no free charges will ever accumulate under quasistatic excitation by a time-varying magnetic field. However, simply knowing the divergence of a vector field does not uniquely define that field. According to the Helmholtz theorem, a unique vector field is only specified if we also know the curl of $\mathbf{J}$ within a simply connected region, as well as its normal component over the boundary [18].

With such criteria in mind, we now turn our attention to Faraday's law, which states:

$$\nabla \times \mathbf{E} = -j\omega \mathbf{B}\,. \tag{4}$$

Given a conductive material with conductivity σ, Ohm's law further states that $\mathbf{J} = \sigma\mathbf{E}$. Note, however, that it is actually much more convenient to express this law in terms of the resistivity function $\rho = 1/\sigma$ such that $\rho\mathbf{J} = \mathbf{E}$. Substitution back into Faraday's law then reveals:

$$\nabla \times (\rho\mathbf{J}) = -j\omega \mathbf{B}\,. \tag{5}$$

Bear in mind that we are explicitly assuming $\rho(x,y)$ might vary as a function of position and therefore cannot be removed from the curl operation as a constant coefficient.

When taken together, (3) and (5) appear to provide a near-complete description for the divergence and curl of $\mathbf{J}$. The only concern is that the curl acts on the quantity $\rho\mathbf{J}$ rather than just $\mathbf{J}$ alone. Fortunately, this does not present a significant challenge in that ρ can be treated as a sectionally-constant function over the domain of interest, thereby dropping out of the curl operation throughout each region. In practice, however, it will be far more convenient to simply leave (5) in its present form and work accordingly.

III. WEAK-EDDY APPROXIMATION

When modeling the excitation of eddy currents, the magnetic field $\mathbf{B}$ is expressed as a linear superposition between two distinct contributions,

$$\mathbf{B} = \mathbf{B}_i + \mathbf{B}_e\,. \tag{6}$$

The first contribution is called the impressed magnetic field $\mathbf{B}_i$ and is interpreted as some arbitrary excitation field imposed onto the system by outside forces. The second contribution is called the induced magnetic field $\mathbf{B}_e$, or simply the eddy field, and is created by the presence of moving charges within our domain of interest. While the impressed field $\mathbf{B}_i$ can be treated as a mathematical given, the eddy field $\mathbf{B}_e$ is dependent on the current distribution $\mathbf{J}$. This relationship is governed by the Biot-Savart law:

$$\mathbf{B}_e(\mathbf{r}) = \frac{\mu_0}{4\pi}\int_V \frac{\mathbf{J}(\mathbf{r}') \times (\mathbf{r} - \mathbf{r}')}{|\mathbf{r} - \mathbf{r}'|^3}\, dV'\,, \tag{7}$$

where $\mathbf{r}$ is an arbitrary observation point and $\mathbf{r}'$ denotes the set of all points inside the volume V that carry electrical current. The complication presented by (7) is that we cannot solve for **J** without first solving for $\mathbf{B}_e$. However, we cannot solve for $\mathbf{B}_e$ unless we also possess a solution for **J**. A complete mathematical solution therefore requires **J** and $\mathbf{B}_e$ to be solved together simultaneously.

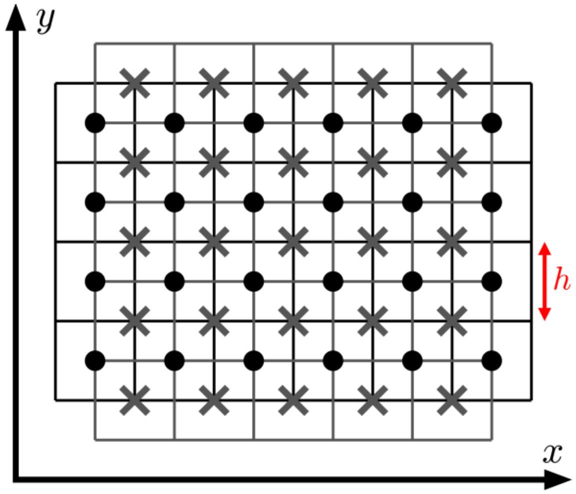

Fig. 2. Staggered mesh positions for sampling vector components of the conduction current density. The Xs denote samples along J_x while dots represent samples along J_y.

Before tackling the simultaneous solution of **J** and $\mathbf{B}_e$, it will first be instructive to consider the special case where $\mathbf{B}_e$ is not a significant factor in relation to $\mathbf{B}_i$. This may occur, for example, when the resistivity ρ is very large, thereby preventing charges from flowing intensely enough to generate any significant self-inductance. A similar situation also occurs when ω is very small, since the changing magnetic fields are too slow to generate significant charge flow. One other scenario occurs when the sheet thickness L_z is very thin, since an infinitely thin sheet of current density technically carries no current. All of these scenarios are mathematically equivalent in that the induced field $\mathbf{B}_e$ is far too weak to compete with the applied magnetic field $\mathbf{B}_i$. In this weak-eddy approximation, the curl equation for **J** may be expressed as:

$$\nabla \times (\rho \mathbf{J}) \approx -j\omega \mathbf{B}_i \quad (|\mathbf{B}_i| \gg |\mathbf{B}_e|)\,. \tag{8}$$

The following sections will first focus exclusively on the weak-eddy approximation by deriving a simultaneous numerical solution to (3) and (8). Doing so will lay the mathematical foundation for discretization of various field components and the subsequent numerical solution that arises. We shall then build on that foundation in later sections by dropping the weak-eddy approximation and deriving a complete numerical solution for **J**.

IV. DISCRETIZATION SCHEME

We begin building our numerical algorithm by establishing a mesh of position coordinates for sampling the vector components J_x and J_y. Figure 2 shows an example of how such a grid might look along a small section of the domain. The Xs denote samples along the J_x function while dots denote samples in J_y. Each sample represents a rectangular block of uniform current density with length and width h but depth L_z. The most important feature of the mesh, however, is the way in which $\mathbf{J}_x$ and $\mathbf{J}_y$ are staggered in space. The significance of this convention will become clear later on when we attempt to calculate the curl and divergence of **J**.

In order to facilitate indexing, it is helpful to define a short-hand notation for each sample along the mesh. We represent the *n*th and *m*th grid samples along *x* and *y* using:

$$x_n = nh \quad (n = 1, 2, 3, \dots)\,, \tag{9}$$
$$y_m = mh \quad (m = 1, 2, 3, \dots)\,. \tag{10}$$

Since the grid samples are staggered from each other in space, it helps to note that half-step increments also satisfy:

$$x_{n+1/2} = (n + 1/2)h\,, \tag{11}$$
$$y_{m+1/2} = (m + 1/2)h. \tag{12}$$

We now reference the staggered mesh of current density through a simple indexed notation given by:

$$J_x^{n,m} = J_x(x_n, y_{m+1/2})\,, \tag{13}$$
$$J_y^{n,m} = J_y(x_{n+1/2}, y_m)\,. \tag{14}$$

V. DIVERGENCE STENCIL

With the sample grid formally defined, we are now ready to approximate (3) in terms of a finite-difference stencil. We begin by dividing the domain into a set of primitive volumes, or cells, each of which is defined by a uniform resistivity ρ_{nm}. An example of such a grid is depicted in Figs. 3 and 4 wherein each cell represents a unique volume denoted as Ω_{nm}. The key is to place all J_x samples on the left and right faces of the cell whereas all J_y samples are placed along the top and bottom. It is also important to note how the far-left and far-right boundaries of the metal plate are occupied only by samples in J_y, with the top and bottom boundaries occupied by samples in J_x. This allows us to implicitly force all normal components of the current density to be zero at the boundaries of the domain, thereby satisfying the last requirement of Helmholtz's theorem. Equivalently, one could also think of this as imposing a Dirichlet boundary condition along the edges of the domain for all normal components to the current density.

We now explicitly write out the divergence of **J** in terms of individual vector components. Recalling the thin-sheet approximation to our model, we let $\partial/\partial z = 0$ so that,

$$\nabla \cdot \mathbf{J} = \frac{\partial J_x}{\partial x} + \frac{\partial J_y}{\partial y} = 0\,. \tag{15}$$

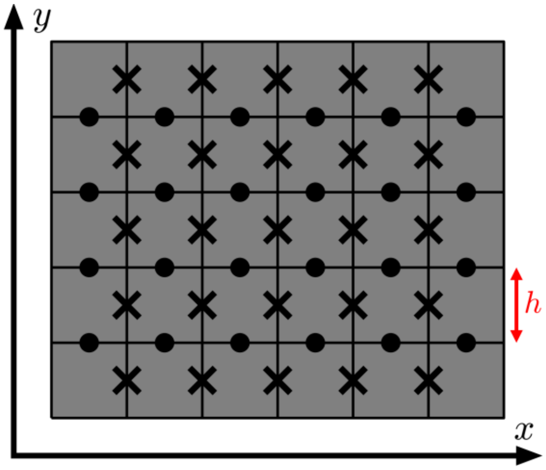

Fig. 3. Divergence mesh with cells of constant resistivity ρ_{nm}.

Applying the central-difference approximation about the $(x_{n+1/2}, y_{n+1/2})$ coordinate then produces:

$$\frac{J_x^{n,m} - J_x^{n-1,m}}{h} + \frac{J_y^{n,m} - J_y^{n,m-1}}{h} = 0\,, \tag{16}$$

or equivalently,

$$J_x^{n,m} - J_x^{n-1,m} + J_y^{n,m} - J_y^{n,m-1} = 0\,. \tag{17}$$

It is interesting to note that we could also obtain an equivalent expression through the use of finite-integration techniques (FIT) [19]. In fact, this is often the preferred method when dealing with variable-coefficient expressions of differential equations [17]. The process begins by calculating the volume integral of (3) over the sub-volume Ω_{nm} to find:

$$\iiint\limits_{\Omega_{nm}} \nabla \cdot \mathbf{J}\, dV = 0\,. \tag{18}$$

By applying the divergence theorem, we can rewrite this expression as the surface integral:

$$\iint\limits_{\partial\Omega_{nm}} \mathbf{J} \cdot d\mathbf{S} = 0\,, \tag{19}$$

where $\partial\Omega_{nm}$ indicates the surface enclosing Ω_{nm} and $d\mathbf{S}$ indicates the outward-pointing differential unit normal to that surface. Since the current density only points along the x- and y-directions, the contributions to the surface integral along $\pm\hat{\mathbf{z}}$ are zero. Furthermore, since each sample in J_x and J_y is assumed to be constant over its respective region, the complete integral evaluates to the simple expression:

$$J_x^{n,m} - J_x^{n-1,m} + J_y^{n,m} - J_y^{n,m-1} = 0\,. \tag{20}$$

which is identical to (17). This shows how FDM and FIT can actually be viewed as two complementary perspectives on the same mathematical problem.

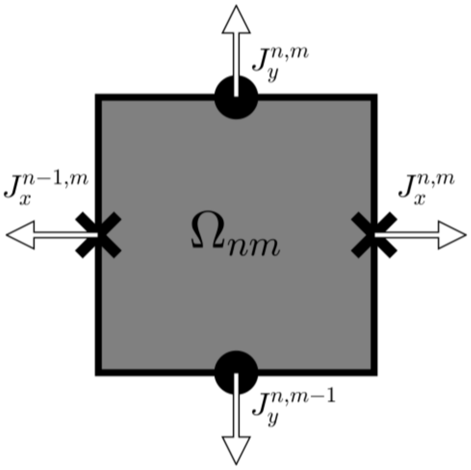

Fig. 4. Individual divergence cell with outward unit normal vectors indicated around the edges.

For the special case of a divergence cell at the far edge of the metal plate, we can implicitly impose boundary conditions by forcing the normal component of the current density to zero. This condition is a direct consequence of (5), which requires that no current be allowed to flow into or out of the edges of the metal plate. For example, at the far-left edge of the metal plate, the $J_x^{n-1,m}$ term contributes nothing and leaves only,

$$J_x^{n,m} + J_y^{n,m} - J_y^{n,m-1} = 0\,. \tag{21}$$

Similar expressions also apply to the top, bottom, and right boundaries of the metal plate as well as the four corner cases.

VI. CURL STENCIL

Looking at the template in Fig. 3, we notice that there are 6×5 divergence cells for a total of 30 divergence equations. However, there are 25 samples in J_x and 24 samples in J_y that need to be calculated. We therefore have only 30 equations with 49 unknowns—an underdetermined system. Speaking more generally, an arbitrary rectangular grid of $N_x \times N_y$ cells will produce $N_d = N_x N_y$ divergence equations. However, the total number of J_x samples is $n_{jx} = (N_x - 1)N_y$, and the total number of J_y samples is $n_{jy} = N_x(N_y - 1)$. The total number of unknown samples N_u is thus:

$$N_u = 2N_x N_y - N_x - N_y\,. \tag{22}$$

This leaves us with a deficit of $N_x N_y - N_x - N_y$ equations before we can arrive at a unique solution.

The reason for our equation deficit is that, as noted earlier, merely specifying the divergence for some vector field does not uniquely define it. It is only when we specify both the divergence and curl simultaneously (as well as the normal component along the boundary) that we produce a uniquely-defined vector field. To that end, we shall next introduce the curl cells depicted in Fig. 5. Unlike the divergence cells, however, the curl cells are shifted in space so that J_y samples now lie on the left and right edges while J_x samples lie at the top and bottom. We may also assume that the total magnetic field B_{nm} throughout each cell is a constant value. To differentiate between curl cells and divergence cells, the regions of curl are denoted with a prime notation using Ω'_{nm}.

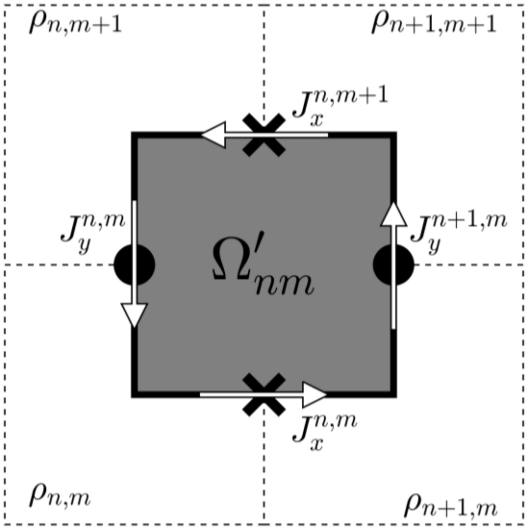

Fig. 5. Individual curl cell with tangential unit vectors indicated. Corresponding resistivity blocks are also indicated.

Unlike the divergence case, a direct finite-difference approximation to (5) is somewhat counter-intuitive due to the product $\rho\mathbf{J}$. This is a classic instance where finite-integration can serve as a more powerful generalization of FDM. Simply begin by calculating the flux integral of (8) across the area within Ω'_{nm} to find:

$$\iint_{\Omega'_{nm}} \nabla \times (\rho\mathbf{J}) \cdot d\mathbf{S} = -j\omega \iint_{\Omega'_{nm}} \mathbf{B}_i \cdot d\mathbf{S}\,, \tag{23}$$

where $d\mathbf{S} = dxdy\ \hat{\mathbf{z}}$ is the differential unit normal across Ω'_{nm}. By applying Stokes' theorem to the left-hand side, we can convert the surface integral into a contour integral with the form:

$$\oint_{\partial\Omega'_{nm}} (\rho\mathbf{J}) \cdot d\boldsymbol{\ell} = -j\omega \iint_{\Omega'_{nm}} \mathbf{B}_i \cdot d\mathbf{S}\ . \tag{24}$$

The contour vectors for $d\boldsymbol{\ell}$ are likewise indicated in Fig. 5 and point along the clockwise direction.

Before we can compute the curl integrals, we must first clarify the sampling along resistivity. Since each sample of current density flows across the boundary between two resistivity cells, there is no clear choice for ρ_{nm} to use with (24). We can solve this problem by simply averaging the two resistivities together along each sample. In terms of our grid stencil, this would could be written as:

$$\rho_x^{n,m} = 0.5\big(\rho_{n,m} + \rho_{n+1,m}\big)\,, \tag{25}$$

$$\rho_y^{n,m} = 0.5\big(\rho_{n,m} + \rho_{n,m+1}\big)\,. \tag{26}$$

Notice how this naturally lends itself to the introduction of anisotropic materials wherein each sample along J_x and J_y has its own resistivity expressed by ρ_x and ρ_y.

We are now ready to apply (24) to the finite-difference stencil. Assuming that each curl cell is excited by a constant magnetic field intensity B_{nm}, the curl expression evaluates to:

$$\begin{aligned}&\rho_y^{n+1,m} J_y^{n+1,m} - \rho_y^{n,m} J_y^{n,m} \\ &\quad + \rho_x^{n,m} J_x^{n,m} - \rho_x^{n,m+1} J_x^{n,m+1} = -j\omega h B_{nm}\,.\end{aligned} \tag{27}$$

Evaluating the above expression over all curl cells will then add $N_c = (N_x - 1)(N_y - 1)$ further equations to our system. When combined with the divergence equations, the total number N_e of equations becomes:

$$N_e = 2N_xN_y - N_x - N_y + 1\,. \tag{28}$$

It is surprising to note that $N_e = N_u + 1$. This seems to indicate one extra equation more than we need, which might lead one to conclude our system is over-determined. Fortunately, the reality is that we actually have one more divergence equation than necessary. To see why, it helps to consider the two equations $a = b$ and $b = c$. Given such information, we can naturally deduce that $a = c$. From the perspective of a linear system, however, any explicit statement of $a = c$ is technically redundant information. By analogy, the set of all divergence equations likewise possesses the same mathematical redundancy. If $N_d - 1$ expressions of divergence are specified, conservation of charge implicitly tells us the flow of current throughout the last grid cell. This means N_xN_y total divergence equations are possible, but only $N_xN_y - 1$ of them contain unique information. We may therefore discard one divergence equation (any one we like, in fact), and the total number of equations becomes:

$$\begin{aligned}N_e &= 2N_xN_y - N_x - N_y \\ &= N_c + N_d - 1.\end{aligned} \tag{29}$$

We now have $N_e = N_u$, and the system is guaranteed a unique solution.

VII. BLOCK MATRIX SOLUTION

To finalize the solution to our eddy current problem, it is necessary to assemble all instances of (17) and (27) into a complete linear system. We begin by collecting all samples of J_x and J_y into the two vectors $\mathbf{u}_x$ and $\mathbf{u}_y$. Recalling that $n_{jx} = (N_x - 1)N_y$ and $n_{jy} = N_x(N_y - 1)$, we can write these vectors as:

$$\mathbf{u}_x = \left[J_x^1, J_x^2, \dots, J_x^{n_{jx}} \right]^T, \tag{30}$$

$$\mathbf{u}_y = \left[J_y^1, J_y^2, \dots, J_y^{n_{jy}} \right]^T. \tag{31}$$

Note that indexing in this context requires a consistent mapping function between every $J_x^{n,m}$ sample on the rectangular grid to a unique J_x^i sample along a linear array. Following the same convention, the forcing vector $\mathbf{b}$ is likewise expressed as:

$$\mathbf{b} = -j\omega h\left[B_1, B_2, \dots, B_{N_c}\right]^T, \tag{32}$$

where each B_i maps to some unique B_{nm} and denotes the constant magnetic field intensity exciting the ith curl cell.

We are now ready to formulate the $N_d - 1$ divergence equations expressed by (17) as a single matrix equation with the form:

$$\mathbf{D}_x\mathbf{u}_x + \mathbf{D}_y\mathbf{u}_y = \mathbf{0}\,, \tag{33}$$

where $\mathbf{D}_x$ and $\mathbf{D}_y$ are called the divergence matrices with $\mathbf{0}$ representing a vector of all zeros. The $\mathbf{D}_x$ matrix has $N_d - 1$ rows and n_{jx} columns, while $\mathbf{D}_y$ has $N_d - 1$ rows and n_{jy} columns. Both matrices are also highly sparse, with only two nonzero elements at most per row.

Moving on to the curl cells, we can assemble all instances of (27) into a system of N_c linear equations. The outcome can also be written as a matrix-vector equation with the form:

$$\mathbf{C}_x\mathbf{u}_x + \mathbf{C}_y\mathbf{u}_y = \mathbf{0}\,, \tag{34}$$

where $\mathbf{C}_x$ and $\mathbf{C}_y$ are called the curl matrices. Both matrices have exactly N_c, but n_{jx} and n_{jy} columns, respectively. If we then combine (33) and (34) together, the result is a block-matrix equation with the form:

$$\begin{bmatrix} \mathbf{C}_x & \mathbf{C}_y \\ \mathbf{D}_x & \mathbf{D}_y \end{bmatrix} \begin{bmatrix} \mathbf{u}_x \\ \mathbf{u}_y \end{bmatrix} = \begin{bmatrix} \mathbf{b} \\ \mathbf{0} \end{bmatrix}. \tag{35}$$

A complete solution is thus found by inverting (35) and extracting all J_x and J_y samples accordingly.

Although the literature does not yet contain any exact solutions for the eddy current density along a metal rectangle, there does exist an exact solution for the weakly-induced eddy current along a metal disk. Given a disk with radius a and conductivity σ, a uniform magnetic field B_0 exciting the disk at a frequency of f will induce the eddy current $\mathbf{J}$ satisfying:

$$\mathbf{J}(r) = -\hat{\boldsymbol{\phi}}\, 2j\pi f\sigma B_0 r/2\,, \tag{36}$$

where r is the radial distance from the center of the disk and $\hat{\boldsymbol{\phi}}$ is the unit angular vector. Note that this expression is true for any thickness L_z since there is no self-inductance to account for.

Figure 6 shows a sample calculation of the weakly-induced eddy current density along a metal disk with 2-cm radius. The frequency of excitation was set to $f = 100$ Hz with a uniform magnetic field intensity of $B_0 = 100$ mT. To mimic the geometry of a disk on a rectangular simulation area, the region inside the disk was set to a conductivity of $\sigma = 1.0$ MS/m while the regions beyond the disk were set to a very small value of only $\sigma = 1.0$ S/m. Note that we cannot directly set $\sigma = 0$ in this region without introducing a singularity into the matrix equation. Looking at (27), a point of zero conductivity would introduce infinite resistivity and thus render the matrix non-invertible. Likewise, the resistivity cannot be set to zero, either, or else similar singularities would ensue.

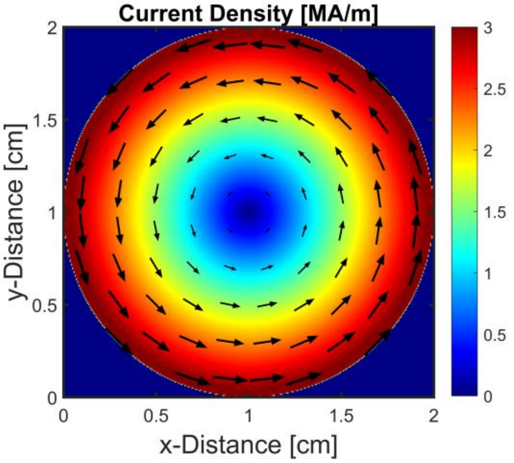

Fig. 6. Induced eddy current density at time $\omega t = \pi/2$ along a metal disk with 2 cm radius and electrical conductivity $\sigma = 1.0$ MS/m. The frequency of excitation is $f = 100$ Hz with a uniform magnetic field intensity of $B_0 = 100$ mT.

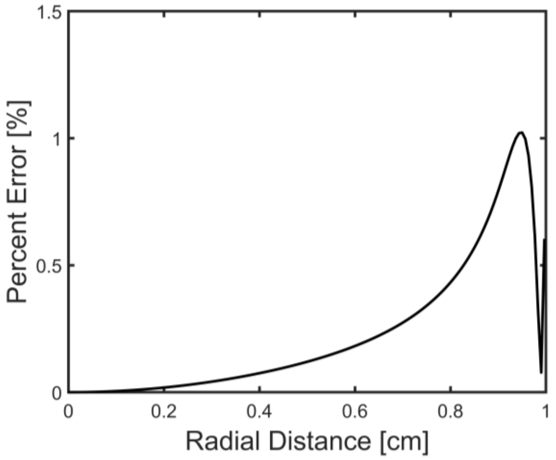

Fig. 7. Percent error between the induced eddy current in Fig. 6 and the analytic expression (36).

For comparison, Fig. 7 plots the percent error as a function of radial distance along the $y = 0$ axis. Since the matrix expression in (35) is highly sparse, the simulation in Fig. 6 could be meshed with an extremely fine resolution of 301×301 cells. The result is very high accuracy in the calculation, with error only reaching 1% near the edge of the disk. This is primarily a result of stair-stepping error that arises from using square cells to approximate a curved boundary, and it is generally unavoidable when utilizing finite-difference schemes that rely on rectangular meshing.

VIII. BLOCK AVERAGING

Once a solution for all J_x and J_y has been obtained, it is often convenient to impose a final post-processing step onto the result. The goal is to adjust the initial placement of samples from a staggered grid onto a consistent grid of positions. Inspired by a similar procedure to that found in [17], one easy way to accomplish this is by simply averaging samples together around the centers of the divergence cells around each Ω_{nm}. The result is a new set of J_x' and J_y' samples that occupy the same position and thus can be plotted meaningfully onto a graphical display. Mathematically, we write this operation as simply,

$$J_x'\left(x_{n+1/2}, y_{m+1/2}\right) = 0.5\left(J_x^{n-1,m} + J_x^{n,m}\right), \qquad (37)$$

$$J_y'\left(x_{n+1/2}, y_{m+1/2}\right) = 0.5\left(J_y^{n,m-1} + J_y^{n,m}\right). \qquad (38)$$

Note how this places the averaged samples along a new grid at the centers of the divergence blocks. Samples along the edge of the domain (e.g., $J_x^{0,m}$) are simply assumed to be zero.

IX. SELF-INDUCTANCE

Let us now consider the implications of self-inductance by dropping the weak-eddy approximation. We express the eddy field $\mathbf{B}_e$ in terms of a magnetic vector potential vector $\mathbf{A}_e$ where $\mathbf{B}_e = \nabla \times \mathbf{A}_e$. The curl equation (5) then satisfies:

$$\nabla \times (\rho \mathbf{J}) + j\omega \nabla \times \mathbf{A}_e = -j\omega \mathbf{B}_i \,. \qquad (39)$$

As we did with (23), we integrate around some arbitrary surface Ω_{nm}' to find:

$$\iint_{\Omega_{nm}'} \nabla \times (\rho \mathbf{J}) \cdot d\mathbf{S} + j\omega \iint_{\Omega_{nm}'} \nabla \times \mathbf{A}_e \cdot d\mathbf{S} = -j\omega \iint_{\Omega_{nm}'} \mathbf{B}_i \cdot d\mathbf{S}. \qquad (40)$$

Applying Stokes' theorem to the left-hand side then leads to:

$$\oint_{\partial\Omega_{nm}'} (\rho \mathbf{J} + j\omega \mathbf{A}_e) \cdot d\boldsymbol{\ell} = -j\omega \iint_{\Omega_{nm}'} \mathbf{B}_i \cdot d\mathbf{S}\,. \qquad (41)$$

Noting the similarity between (24) and (41), we have only to account for the vector potential field expressed by $\mathbf{A}_e$. This is accomplished by sampling the *x*- and *y*-components of $\mathbf{A}_e$ along the same staggered grid as J_x and J_y. Assuming constant values throughout each cell, we quickly find:

$$\begin{array}{ll} +\rho_y^{n+1,m} J_y^{n+1,m} & -\rho_y^{n,m} J_y^{n,m} \\ +\rho_x^{n,m} J_x^{n,m} & -\rho_x^{n,m} J_x^{n,m+1} \\ +j\omega A_y^{n+1,m} & -j\omega A_y^{n,m} \\ +j\omega A_x^{n,m} & -j\omega A_x^{n,m+1} = -j\omega h B_{nm}. \end{array} \qquad (42)$$

The immediate consequence of accounting for the eddy fields in A_x and A_y is that we have now doubled the number of unknowns in our linear system. We therefore need another N_u equations in order to maintain a unique solution. This is accomplished by expressing the Biot-Savart law in terms of magnetic vector potential using [20]:

$$\mathbf{A}_e(\mathbf{r}) = \frac{\mu_0}{4\pi} \int \frac{\mathbf{J}(\mathbf{r}')}{|\mathbf{r} - \mathbf{r}'|} dV' \,. \qquad (43)$$

Splitting the fields into *x*- and *y*-components, we may explicitly write this as:

$$\mathrm{A}_x(\mathbf{r}) = \frac{\mu_0}{4\pi} \int \frac{J_x(\mathbf{r}')}{|\mathbf{r} - \mathbf{r}'|} dV', \qquad (44)$$

$$\mathrm{A}_y(\mathbf{r}) = \frac{\mu_0}{4\pi} \int \frac{J_y(\mathbf{r}')}{|\mathbf{r} - \mathbf{r}'|} dV' \,. \qquad (45)$$

The importance of (44) and (45) is that we can now derive the necessary information for a unique solution. Using the finite-difference stencil as a guide, we express each integral as a finite sum along each grid cell in the domain. Recalling that each sample in J_x and J_y is represented as a uniform block of length/width h and a thickness L_z, we write out each vector potential sample as:

$$A_x^{n,m} = \frac{\mu_0 h^2 L_z}{4\pi} \sum_{\ell,k} \frac{J_x^{\ell,k}}{\sqrt{(x_\ell - x_n)^2 + (y_\ell - y_k)^2}}, \qquad (46)$$

$$A_y^{n,m} = \frac{\mu_0 h^2 L_z}{4\pi} \sum_{\ell,k} \frac{J_y^{\ell,k}}{\sqrt{(x_\ell - x_n)^2 + (y_\ell - y_k)^2}}. \qquad (47)$$

A special exception occurs when $\ell = n$ and $k = m$. In this case, we need to evaluate the full integral,

$$\int_{-L_z/2}^{+L_z/2} \int_{-h/2}^{+h/2} \int_{-h/2}^{+h/2} \frac{dx\,dy\,dz}{\sqrt{x^2 + y^2 + z^2}} \,. \qquad (48)$$

It is unfortunate that the above expression has no closed-form solution. It can, however, be evaluated numerically with arbitrary degrees of precision. For this work, we found that the basic midpoint rule provides reasonable accuracy in a short amount of time.

With the addition of (44) and (45), we are now ready to express the complete solution with self-inductance.

Begin by defining the unknown vectors $\mathbf{a}_x$ and $\mathbf{a}_y$ in a similar vein to $\mathbf{u}_x$ and $\mathbf{u}_y$ such that,

$$\mathbf{a}_x = \left[A_x^1, A_x^2, \dots, A_x^{n_{jx}}\right]^T, \tag{49}$$

$$\mathbf{a}_y = \left[A_y^1, A_y^2, \dots, A_y^{n_{jy}}\right]^T. \tag{50}$$

This now allows us to simultaneously solve for every A_x and A_y sample alongside the J_x and J_y. Writing out the complete system of equations, we find a block-matrix equation with the form of:

$$\begin{bmatrix} \mathbf{C}_x & \mathbf{C}_y & \mathbf{N}_x & \mathbf{N}_y \\ \mathbf{D}_x & \mathbf{D}_y & \mathbf{0} & \mathbf{0} \\ \mathbf{M}_x & \mathbf{0} & \mathbf{I} & \mathbf{0} \\ \mathbf{0} & \mathbf{M}_y & \mathbf{0} & \mathbf{I} \end{bmatrix} \begin{bmatrix} \mathbf{u}_x \\ \mathbf{u}_y \\ \mathbf{a}_x \\ \mathbf{a}_y \end{bmatrix} = \begin{bmatrix} \mathbf{b} \\ \mathbf{0} \\ \mathbf{0} \\ \mathbf{0} \end{bmatrix}, \tag{51}$$

where $\mathbf{I}$ denotes an identity matrix and $\mathbf{0}$ indicates a matrix (or vector) of all zeros. The matrices $\mathbf{N}_x$ and $\mathbf{N}_y$ can be referred to as the vector-potential matrices, or perhaps the self-inductance matrices, because they arise from the added self-inductance terms in (42). Like the curl matrices $\mathbf{C}_x$ and $\mathbf{C}_y$, these matrices are highly sparse and therefore add little in terms of computational complexity. The last two matrices, $\mathbf{M}_x$ and $\mathbf{M}_y$, are called the Biot-Savart matrices and express the information contained by (46) and (47). Unfortunately, these matrices are completely full and therefore add significant computational cost to the final inversion. The result, however, is a complete expression of eddy current density **J** along the metal sheet with full account taken for self-inductance.

An immediate concern with the matrix equation described by (51) is the presence of four scalar fields that need to be solved for simultaneously. Fortunately, we are not really interested in the actual solutions for $\mathbf{a}_x$ and $\mathbf{a}_y$ and can thus remove them through simple substitution. The resulting matrix equation is a far more compact expression given by:

$$\begin{bmatrix} (\mathbf{C}_x - \mathbf{N}_x\mathbf{M}_x) & (\mathbf{C}_y - \mathbf{N}_y\mathbf{M}_y) \\ \mathbf{D}_x & \mathbf{D}_y \end{bmatrix} \begin{bmatrix} \mathbf{u}_x \\ \mathbf{u}_y \end{bmatrix} = \begin{bmatrix} \mathbf{b} \\ \mathbf{0} \end{bmatrix}. \tag{52}$$

A key advantage to (52) is that the system matrix is entirely geometry-dependent. It therefore need only be inverted once, and the resulting eddy currents can be calculated rapidly under any arbitrary forcing function contained within **b**. This can be especially useful when tracking the trajectory of a metal particle as it passes over an eddy current separator. Each small increment in time requires a fresh calculation of force and torque due to changes in $\mathbf{B}_\mathrm{i}$ over position. Fortunately, the system matrix remains identical with each step and thus does not require repeated inversions.

X. VALIDATION

To validate the numerical algorithm presented here, we ran a side-by-side comparison between FDM and the Computer Simulation Technology (CST) EM Studio software suite [21]. The model was comprised of a rectangular metal sheet defined by the physical dimensions $L_x = 2.0$ cm, $L_y = 1.0$ cm, and $L_z = 0.1$ cm with a conductivity of $\sigma = 5.0$ MS/m. The magnetic field exciting the sheet was set to a uniform field profile with amplitude $B_0 = 100$ mT at a frequency of $f = 10$ kHz.

Figure 8 shows the results of the two simulations when sampled at a grid spacing of $h = 0.5$ mm. Since the induced currents are strongly out of phase with the applied field, the results had to be shifted in phase by 90° before rendering the real part of **J**. For a more precise inspection, Fig. 9 shows both the real and imaginary components of J_y at $t = 0$ along a horizontal cut through the center of the rectangular sheets.

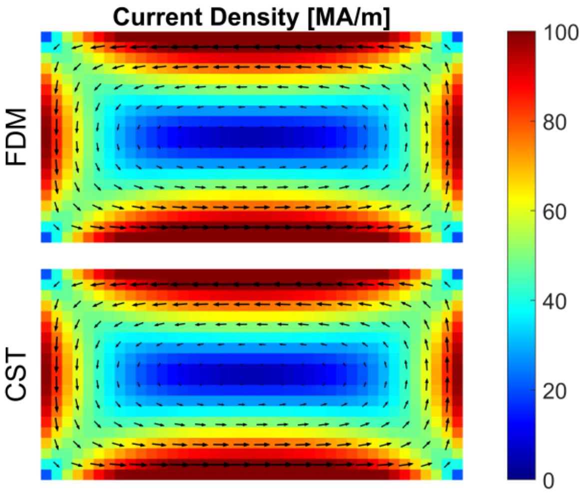

Fig. 8. Induced eddy currents in a thin metal sheet at phase angle $\phi = 90°$. The top solution was calculated using FDM and the bottom solution was calculated using commercial software (CST).

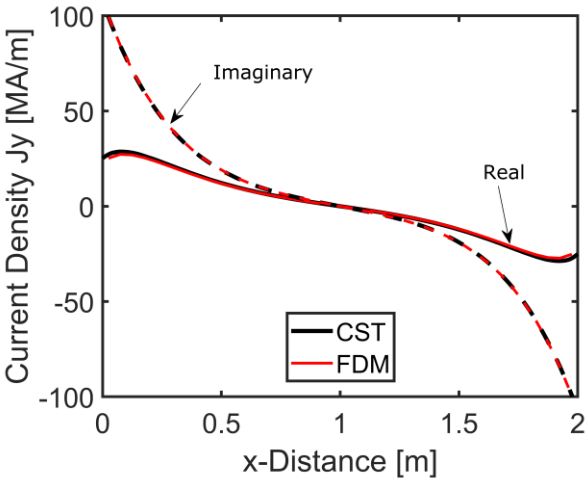

Fig. 9. Real and imaginary components of J_y at $t = 0$ along a horizontal cut down the center of the rectangular metal sheet.

Results from the comparison show very strong agreement, thereby validating the finite-difference approach to eddy current calculations. Any errors in the FDM calculation are primarily the result of using rectangular blocks of constant current density to approximate the true values within. Other errors also accumulate from imperfections in the numerical integration used to solve (44) and (45), as well as the thin-sheet approximation. The key metric of interest, however, is computational time. Since CST is based on the $\mathbf{A}-\varphi$ formalism, a thin metal sheet had to be placed within a three-dimensional void of empty space. As a result, the total number of elements was quite large (31,031 tetrahedrons), and a typical simulation required approximately 60 seconds to complete on a standard laptop computer. In contrast, the FDM model need only sample the metal sheet in isolation and thus required only 800 divergence cells. Consequently, the total time to build the system matrix and solve for the current density was barely 0.5 seconds using standard Matlab subroutines.

XI. DISCUSSION

Although this work has focused exclusively on the problem of thin metal sheets, there is no reason why it cannot be expanded out to a complete, three-dimensional formalism. Such an algorithm would have a distinct advantage over potential-based formalisms in that the simulation boundary can terminate at the edge of a body of interest. The key trade-off, however, is a forfeiture of the sparse system matrix that must be inverted. Since every sample in the FDM algorithm is dependent on every other sample, the resulting system matrix is necessarily going to be full. This means the computational complexity is necessarily $O(N^3)$ when using Gauss-Jordan elimination to invert an $N \times N$ system matrix. In the future, however, it may be possible to circumvent this limitation through iterative-based inversion methods rather than direct inversion of the full matrix.

ACKNOWLEDGEMENTS

This work was funded by the United States Advanced Research Project Agency-Energy (ARPA-E) METALS Program under cooperative agreement grant DE-AR0000411. The author would also like to thank Professor Raj Rajamani, Jaclyn Ray, and Dawn Sweeney for their insightful edits and proof-reading.

REFERENCES

[1] C. V. Dodd and W. E. Deeds, “Analytical solutions to eddy-current probe-coil problems,” *Journal of Applied Physics*, vol. 39, no. 6, pp. 2829-2838, 1968.

[2] J. R. Bowler, “Eddy-current interaction with an ideal crack. 1: The forward problem,” *Journal of Applied Physics*, vol. 75, no. 12, pp. 8128-8137, 1994.

[3] E. C. Okress, D. M. Wroughton, G. Comenetz, P. H. Brace, and J. C. R. Kelly, “Electromagnetic levitation of solid and molten metals,” *Journal of Applied Physics*, vol. 23, no. 5, pp. 545-552, 1952.

[4] E. Fromm and H. Jehn, “Electromagnetic forces and power absorption in levitation melting,” *British Journal of Applied Physics*, vol. 16, no. 5, pp. 653-662, 1965.

[5] F. Maraspin, P. Bevilacqua, and P. Rem, “Modelling the throw of metals and nonmetals in eddy current separations,” *International Journal of Mineral Processing*, vol. 73, no. 1, pp. 1-11, 2004.

[6] N. Dholu, J. R. Nagel, D. Cohrs, and R. K. Rajamani, “Eddy current separation of nonferrous metals using a variable-frequency electromagnet,” *KONA Powder and Particle Journal*, vol. 34, pp. 241-247, 2017.

[7] Y. R. Smith, J. R. Nagel, and R. K. Rajamani, “Electrodynamic eddy current separation of end-of-life PV materials,” in *In: Zhang L. et al. (eds) Energy Technology 2017. The Minerals, Metals & Materials Series.*, Cham, Springer, 2017, pp. 379-386.

[8] J. D. Ray, J. R. Nagel, D. Cohrs, and R. K. Rajamani, “Forces on particles in time-varying magnetic fields,” *KONA Powder and Particle Journal*, vol. 35, pp. 251-257, 2018.

[9] J. R. Nagel, “Induced eddy currents in simple conductive geometries,” *IEEE Antennas and Propagation Magazine*, vol. 60, no. 1, pp. 81-88, 2018.

[10] G. Sinha and S. S. Prabhu, “Analytical model for estimation of eddy current and power loss in conducting plate and its application,” *Physical Review Special Topics: Accelerators and Beams*, vol. 14, no. 6, p. 062401, 2011.

[11] G. Lohofer, “Theory of an electromagnetically levitated metal sphere I: Absorbed power,” *SIAM Journal on Applied Mathematics*, vol. 49, no. 2, pp. 567-581, 1989.

[12] T. P. Theodoulidis, N. V. Kantartzis, T. D. Tsiboukis, and E. E. Kriezis, “Analytical and numerical solution of the eddy-current problem in spherical coordinates based on the second-order vector potential formulation,” *IEEE Transactions on Magnetics*, vol. 33, no. 4, pp. 2461-2472, 1997.

[13] J. Chen, Z. Chen, C. Tao, and L.-B. Zhang, “An adaptive finite element method for the eddy current model with circuit/field couplings,” *SIAM Journal on Scientific Computing*, vol. 32, no. 2, pp. 1020-1042, 2010.

[14] O. Biro and K. Preis, “On the use of the magnetic vector potential in the finite-element analysis of three-dimensional eddy currents,” *IEEE Trans-*

actions on Magnetics, vol. 25, no. 4, pp. 3145-3159, 1989.

[15] M. R. Krakowski, "On certain properties of the electric vector potential in eddy-current problems," *IEE Proceedings A - Physical Science, Measurement and Instrumentation, Management and Education - Reviews*, vol. 134, no. 10, pp. 768-772, 1987.

[16] A. Krawczyk and J. A. Tegopoulos, *Numerical Modelling of Eddy Currents*. Oxford: Clarendon Press, 1993.

[17] J. R. Nagel, "Numerical solutions to Poisson equations using the finite-difference method," *IEEE Antennas and Propagation Magazine*, vol. 56, no. 4, pp. 209-224, 2014.

[18] G. B. Arfken and H. J. Weber, *Mathematical Methods for Physicists*. 5th ed., New York: Academic Press, 2001.

[19] M. Clemens and T. Weiland, "Discrete electromagnetism with the finite integration technique," *Progress In Electromagnetics Research*, vol. 32, pp. 65-87, 2001.

[20] J. D. Jackson, *Classical Electrodynamics*. 3rd ed., Hoboken (NJ): Wiley, 1999.

[21] Computer Simulation Technology, "CST EM Studio," [Online]. Available: www.cst.com. [Accessed 2016].

James R. Nagel studied Electrical Engineering at the University of Utah in Salt Lake City and earned his Ph.D. in 2011. He now works as a Research Associate for the University of Utah where he studies magnetic separation methods for scrap metal recycling.